

Simulation of the Francis-99 Hydro Turbine During Steady and Transient Operation

Yuvraj Dewan

Senior Application Engineer, CD-adapco. 200 Shepherds Bush Road, London W6 7NL, UK

E-mail: yuvraj.dewan@cd-adapco.com

Chad Custer

Technical Specialist: Turbomachinery, CD-adapco. 21800 Haggerty Road, Northville, MI-48335, USA

E-mail: chad.custer@cd-adapco.com

Artem Ivashchenko

Project Engineer, Mechanical Solutions Inc. 11 Apollo Drive, Whippany, NJ 07981, USA

E-mail: artem.ivashchenko@mechsol.com

Abstract. Numerical simulation of the Francis-99 hydroturbine with correlation to experimental measurements are presented. Steady operation of the hydroturbine is analyzed at three operating conditions: the best efficiency point (BEP), high load (HL), and part load (PL). It is shown that global quantities such as net head, discharge and efficiency are well predicted. Additionally, time-averaged velocity predictions compare well with PIV measurements obtained in the draft tube immediately downstream of the runner. Differences in vortex rope structure between operating points are discussed.

Unsteady operation of the hydroturbine from BEP to HL and from BEP to PL are modeled. It is shown that simulation methods used to model the steady operation produce predictions that correlate well with experiment for transient operation.

Time-domain unsteady simulation is used for both steady and unsteady operation. The full-fidelity geometry including all components is meshed using an unstructured polyhedral mesh with body-fitted prism layers. Guide vane rotation for transient operation is imposed using fully-conservative, computationally efficient mesh morphing. The commercial solver STAR-CCM+ is used for all portions of the analysis including meshing, solving and post-processing.

1. Introduction

According to the 2016 Global Status Report on renewable energy, in 2015 over 23% of global power production came from renewable energy sources, of which over 57% were hydropower sources [1]. Most of that capacity belongs to large hydroelectric plants using Francis turbines to generate that power. Furthermore, some countries, such as Iceland, Brazil, Canada and Norway, derive a significant majority of their electric power from hydroelectric plants. As a result, smooth and continuous operation of Francis turbines and a thorough understanding of



the fluid flow inside a turbine at best efficiency point and off-design conditions is important for hydropower producers.

Advancements in computational fluid dynamics (CFD) have contributed greatly to component design [2, 3] and performance prediction of Francis turbines. This paper focuses on the use of CFD for performance prediction and detailed characterization of the flow-field. The experimental processes involved in performance prediction of the complete turbine system from scroll to draft tube are expensive, time-consuming and demanding in terms of manpower. By comparison, a CFD analysis of the turbine system is faster and, once a model is created, can produce additional results with very little effort. Still, due to constraints on computational power, many simulations have been performed with coarse meshes and steady state methods. With this method, moving components of the turbine are modeled with moving reference frames (MRF) instead of physically rotating the runner mesh relative to the mesh of stationary components [4, 5, 6, 7]. While undoubtedly useful for clarification of a wide variety of issues, such analyses fail to capture important transient events, such as vortex rope development, wake interactions and pressure oscillations, especially at off-design conditions. Additionally, these unsteady effects influence global, time-averaged quantities, which limits the accuracy of steady simulation methods. Thankfully, continuous advancements in both commercial CFD codes and, more importantly, in processing power and its cost have made mesh refinement and unsteady rigid body motion (RBM) possible for a wider audience of engineers and researchers [8, 9, 10].

This paper presents the results of unsteady CFD analysis of the Francis-99 test case. Three operating conditions, including two off-design conditions, are simulated. The turbine was modeled from the inlet of the scroll to the discharge of the draft tube into the tank, using upwards of 15 million cells. Analysis was conducted using the commercial code STAR-CCM+ produced by CD-adapco [11]. The results are compared against the data gathered by the researchers at the Norwegian Hydropower Center (NVKS).

2. Reference Experiment

The Francis-99 hydroturbine is an experimental test rig housed at the Norwegian Hydropower Center (NVKS) at the Norwegian University of Science and Technology (NTNU). The experiment contains a scaled down turbine which is based on the characteristics of the turbines found at the Tokke hydroelectric powerstation in Telemark, Norway. It has been scaled down from the actual operation scale to lab scale. Numerous experimental investigations have been performed including the characterization of steady operation at numerous operating conditions, load acceptance and rejection, emergency shutdown, total load rejection, and runaway.

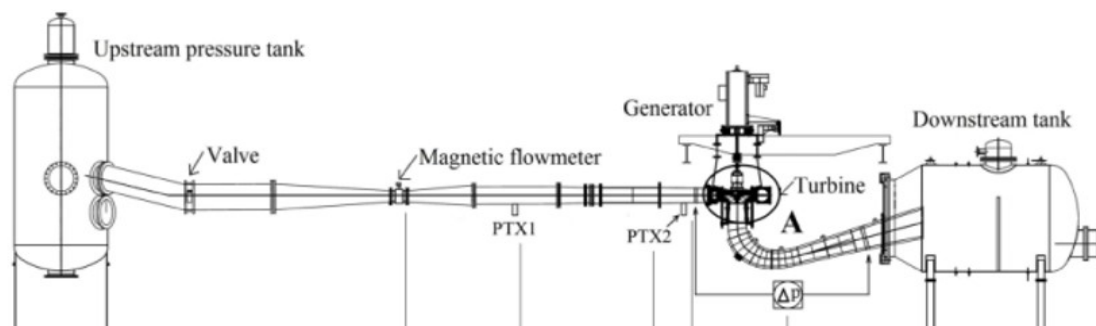


Figure 1: Francis-99 experimental setup schematic [12]

Geometric CAD data, operating conditions and experimental measurements are provided online for steady operation at BEP, PL and HL [12]. Additionally, transient operation for BEP to HL and BEP to PL conditions are characterized. This open access has facilitated numerous

numerical investigations that are part of the continuing Francis-99 workshop series. The main global quantities of interest such as net head, discharge and hydraulic efficiency are measured for both steady and unsteady operation. Additionally, velocity measurements in the draft tube just downstream of the runner are obtained using PIV for steady operation conditions as indicated by the solid lines in Figure 2. Simulation data will be correlated to these experimental data.

3. Simulation Setup

3.1. Geometry

The geometry for the Francis-99 turbine is openly provided by the Francis-99 committee in a variety of CAD and mesh formats [12]. For this study, the STEP format of the geometry is used. The simulation domain consists of 4 main regions: spiral casing, guide vanes, runner and draft tube. The entirety of the simulation domain is shown in Figure 2a and a view of the runner is shown in Figure 2b.

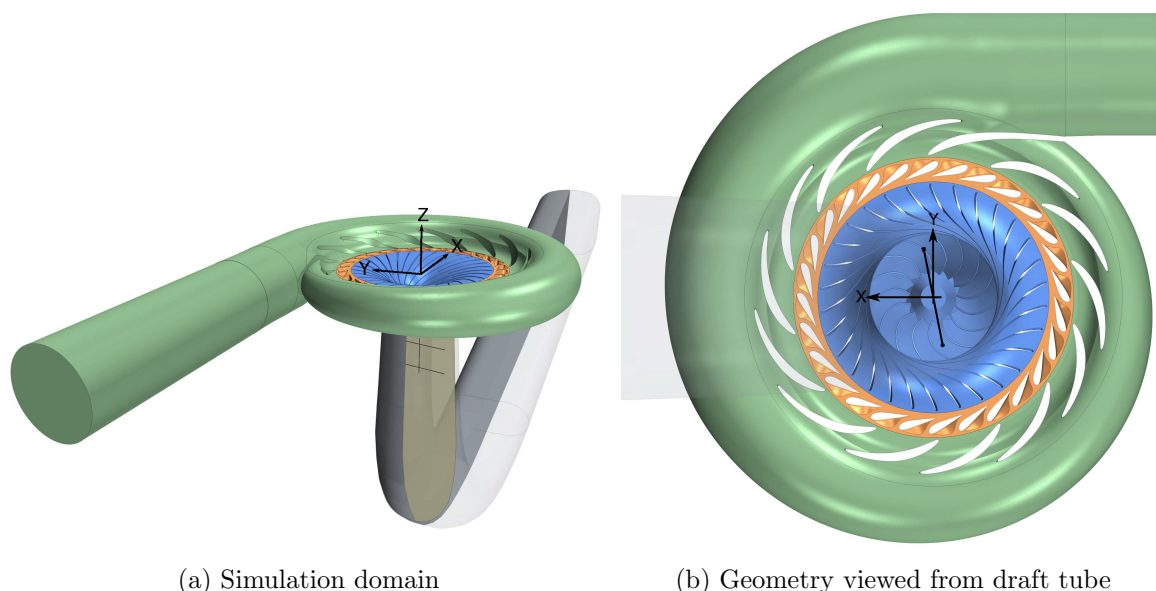


Figure 2: Francis-99 CAD geometry shown with the global coordinate system and PIV measurement line locations

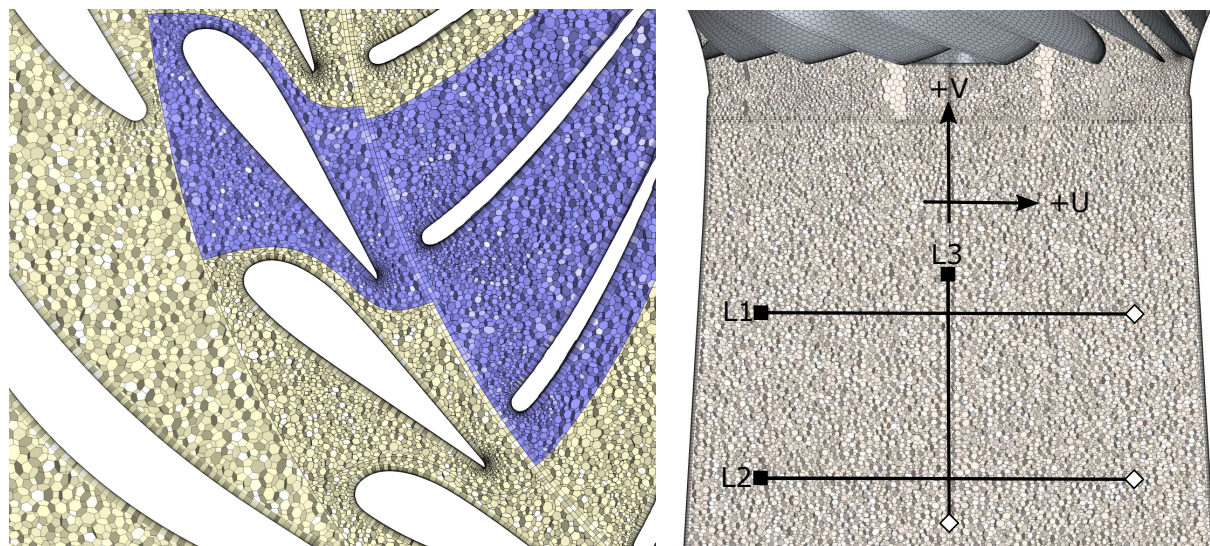
No CAD defeaturing is performed. All geometric details including fillets, chamfers, and small edges provided in the CAD are retained in the model. No secondary flows, such as the seals between runner and casing, were provided and so are not included in the simulation domain.

3.2. Computational Mesh

A polyhedral mesh with prism layers is generated for the entire domain. A polyhedral cell is an unstructured mesh topology where each cell can have an arbitrary number of faces. This increases cell connectivity to neighbors and increases the degrees of freedom available to the mesher. As a result, higher quality cells can be obtained with low skewness and smooth volumetric growth. Consequently, the polyhedral mesh technology generally shows better convergence than a tetrahedral mesh for a given number of cells [13].

In addition to the numerical benefits of the polyhedral cell, the topology allows for better modeling of the physics and geometry of the system. The unstructured nature of the mesh allows for arbitrarily complex geometry to be modeled without the need for geometric simplification. The polyhedral mesh is well suited to flows in which there is no clear flow direction, such as

the vortex rope. With many more faces than a structured or tetrahedral mesh, faces with the largest face flux are generally closer to normal to the velocity field, resulting in better stability and lower error. Figure 3b shows the uniform and direction-independent nature of the mesh in the draft tube immediately downstream of the runner.



(a) Midspan mesh of bladed components showing duplicated periodic sector

(b) Draft tube mesh downstream of runner with velocity measurement locations and directions

Figure 3: Polyhedral mesh with prism layers used to discretize domain

A layer of thin, anisotropic cells, known as prism layers, are grown outward from all wall surfaces. These prism layers accurately capture the large gradients in the flow-field approaching the no-slip condition imposed at the wall. The prism layer mesh at mid-span of the bladed components is shown in Figure 3a. Ten prism layers are used at all wall surfaces. The specified first cell thickness is set such that the wall y^+ is generally less than five. For the BEP operating point, the average y^+ for all wall boundaries in the domain is 4.5. In addition to the prism layers used to capture the wall gradients, one thick prism layer is used at the interface between all rotating and stationary regions. This ensures cell orthogonality and consistent sizing at the interface.

To maintain self-similarity, each periodic and symmetry section is meshed once, then repeated. As shown in Figure 3a, only one guide vane and runner flow passage is meshed, then the resulting grids are duplicated, patterned and conformally fused into a unified domain. Likewise, one half of the spiral casing and draft tube is meshed and mirrored about the plane of symmetry and fused. Approximately 14M cells are used to model the complete domain. The bladed components represent the largest cell count with approximately 4M cells used to mesh the guide vanes and 5M cells used to mesh the runner. The spiral casing and draft tube consists of 3.5M cells and 1.3M cells, respectively.

3.3. Boundary Conditions

3.3.1. Steady Operation From the experimental measurements, both the flow rate and pressure at the spiral casing inlet are observed to be unsteady. The unsteadiness observed at this location is due to the dynamics of the system including the blade passing effects. The phase lock between the observed oscillations at the measurement locations relative to the runner position is not

available. For these reasons, constant values are imposed as boundary conditions for steady operation. A consequence of specifying constant values for boundary conditions is that some of the observed oscillations will be artificially damped. To accurately model the oscillations observed at the measurement locations, the domain must be extended to a secondary station where values are known to be constant. This is neither feasible, or necessary. The effect of imposing constant values as boundary conditions for the steady operation case does not greatly influence the quantities of interest.

With it established that constant values will be used for the boundary conditions of the steady operation cases, the type of boundary condition imposed at the inlet and outlet must be determined. The measurement of static pressure is often more reliable than that of flow rate. Additionally, the static pressure at the inlet of a Francis turbine is usually well known based on the vertical elevation change from the inlet of the turbine to free surface of the water powering the turbine. For these reasons, a pressure condition will be used as the inlet condition. Total pressure is specified as the inlet boundary condition as given by equation 1.

$$P_{t1} = P_1 + \frac{1}{2}\rho \left(\frac{Q}{A_1}\right)^2 \quad (1)$$

With total pressure fixed at the inlet, the outlet boundary condition can be imposed as either a constant static pressure, or discharge. Again, it is common to have reliable data for the outlet static pressure of a Francis turbine. Additionally, the relative pressure difference from inlet to outlet is strongly linked to net head, which greatly influences performance. For these reasons a constant value of static pressure is imposed at the domain outlet. All other required boundary values are extrapolated from the interior of the domain. The test rig measures the outlet static pressure using a ring manifold as specified in the IEC 60193 standard [14]. However, this pressure is measured at a section upstream of the domain, not at the location where boundary conditions will be specified. Consequently, the measured pressure must be adjusted before it is applied as a boundary condition. The static pressure applied at the downstream boundary is approximated using Bernoulli's principle as given in equation 2. Let 1 be the measurement plane and 2 be the domain outlet.

$$P_1 + \frac{1}{2}\rho v_1^2 + \rho g z_1 = P_2 + \frac{1}{2}\rho v_2^2 + \rho g z_2 \quad (2)$$

The velocity at each section can be estimated using the continuity equation. The area for each location is measured in STAR-CCM+ and the value for discharge is taken from the operating condition.

$$Q = vA \quad (3)$$

The absolute static pressure at the outlet can be calculated by combining equations 2 and 3.

$$P_2 = P_1 + \rho \left[\frac{Q^2}{2} \left(\frac{1}{A_1^2} - \frac{1}{A_2^2} \right) + g(z_1 - z_2) \right] \quad (4)$$

The provided value for gravitational acceleration (g) and density (ρ) are 9.82 m/s^2 and 999.8 kg/m^3 , respectively. The difference in the vertical positions ($z_1 - z_2$) is measured from the CAD to be 0.4031 m . The cross sectional areas A_1 and A_2 are measured from the CAD to be 0.2292 m^2 and 0.3294 m^2 , respectively. The discharge (Q) and measured outlet pressure (P_1) are provided from the experimental data. While running the simulations, it was confirmed that the outlet pressure measured in the experiment matched well with the pressure at the measurement plane after the outlet corrections.

3.3.2. Transient Operation

Inlet For the transient operating conditions, the inlet pressure is specified as a function of time. The inlet pressure profile provided from the experiment must be processed before it is applied to the simulation. The inlet pressure data provided contains high frequency content related to the blade passing frequency and sampling noise. This high frequency content is filtered using seasonal decomposition with moving averages [15].

An additive model is used for the seasonal decomposition, meaning that the original signal is divided into the following components: trend, seasonal and error. The sum of these components returns the original signal. The trend component is first calculated using a symmetric moving average. This provides the long-term or low frequency trends in the data. The original signal is then 'de-trended' by subtracting the trend component. The 'de-trended' data is then corrected to a zero mean to give the seasonal component. This component provides the high frequency content from the original data. Finally, the error component is calculated by taking the difference between the original signal and the sum of the trend and seasonal components. This error component represents the noise and turbulence in the data. Figure 4 shows the decomposition of inlet pressure at the load acceptance transient operating condition (BEP to HL). The trend component is the boundary condition that is applied for simulation.

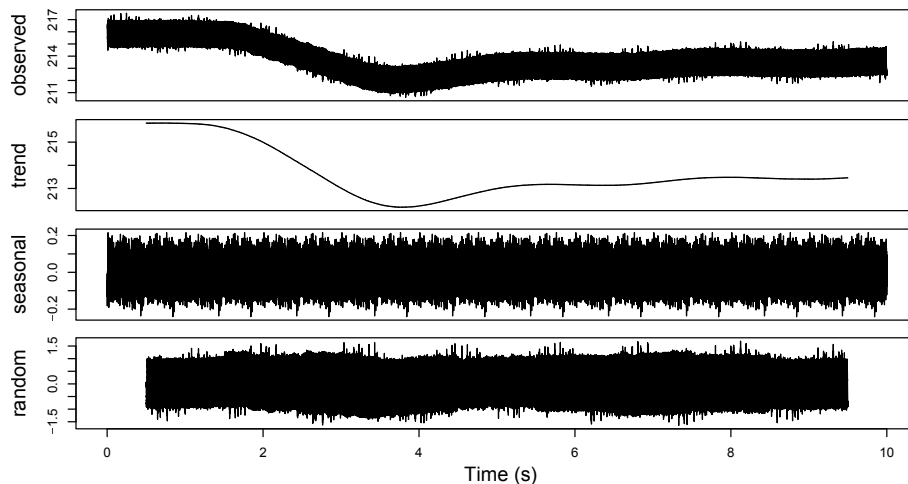


Figure 4: Time series decomposition of the inlet pressure for the load acceptance condition. Units for all y axes are kPa

Outlet Measured static pressure at the outlet measurement plane is not directly provided from the experiment for the transient operation cases. The net head (H), discharge (Q) and inlet static pressure (P_1) are provided as functions of time for the transient operation case. The static pressure at the measurement plane is calculated from the provided quantities using the definition of net head as given in equation 5 and the relation between discharge, area and velocity given in equation 3.

$$H = \frac{P_1 - P_2}{\rho g} + \frac{v_1^2 - v_2^2}{2g} + z \quad (5)$$

This calculated static pressure is then corrected for application at the boundary condition location as given in equation 4.

3.4. Solver Setup

A Semi-Implicit Method for Pressure-Linked Equations (SIMPLE) algorithm is used to solve the incompressible Reynolds-Averaged Navier-Stokes equations. Spatial gradients are computed to second-order accuracy and a second-order, implicit unsteady method is used to advance time. Rotation is modeled using rigid body motion (RBM) with in-place, direct interfaces between rotating and stationary regions that are recomputed at each time-step. A time-step corresponding to one degree of rotation is used and twenty inner iterations are used to converge each time-step. Menter's SST $k - \omega$ turbulence model is used with an all $y+$ implementation. However, as discussed in Section 3.2, the mesh was generated so that a low $y+$ treatment is used on the vast majority of wall boundaries.

3.5. Guide Vane Motion

For transient operating conditions, each guide vane rotates about its own axis as a function of time defined by a piece-wise linear rotation profile. This motion is modeled by a mesh morphing approach. The walls of each guide vane are set to rigidly rotate as specified by the transient operation of the turbine. Hub and shroud boundaries of the guide vane region are set to a 'floating' condition which allows the mesh on these boundaries to freely adjust to the motion applied to the other boundaries. Inlet and outlet interface boundaries to the guide vanes are fixed. This method is fully conservative and computationally efficient. Remeshing of the domain is not required and there is no interpolation of the solution from one time-step to the next. Figure 5 shows the starting and final guide vane position for the load reduction condition.

Another approach that could be implemented for guide vane motion is the Overset or Chimera grid approach [16]. In this technique, every component which has relative motion to another is meshed independently. This leads to a series of overlapping meshes. At each time-step, all of the overlapping grids are combined into a single grid on which the physical equations are solved. The details of this mesh combination is outside the scope of this report. For this study, each guide vane would require its own Overset (or overlapping) region. This means that each guide vane region needs an interface with the background region and two of its neighboring guide vanes, which would result a total of 57 overset interfaces that need to be resolved at each time step. There is a high computational expense associated with the computation of a large number of interfaces, and it is the reason that the morphing approach is preferred for this study.

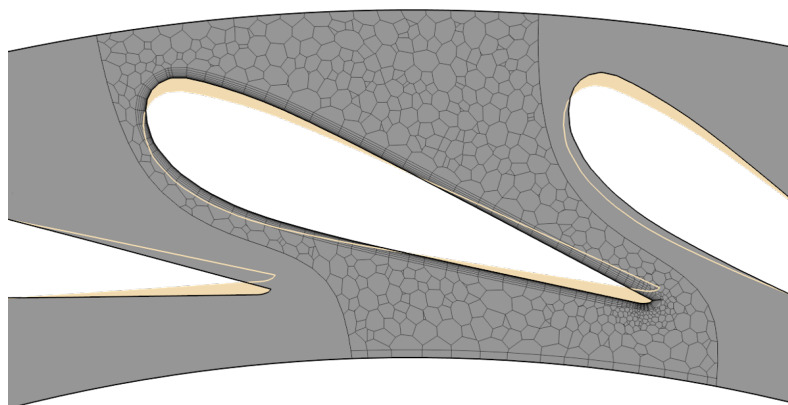


Figure 5: Guide vane position at BEP (grey mesh) and PL (cream).

4. Results

4.1. Steady Operation

A simulation was run for each of the three operating conditions that are documented in the reference experiment (PL, BEP and HL). The simulation was run long enough for integral quantities to reach cycle steady values. The amount of time taken for each operating condition to reach cycle steady behavior is variable. The PL case exhibits certain low frequency trends, which requires the solution to be run over a longer period of time. The HL case requires a shorter run time to reach convergence, and the BEP case even shorter.

Figure 6 shows the predicted values of the integral quantities as compared to the reference experiment. The simulation predictions for all of the relevant quantities of interest agree well with experiment across all three steady operating conditions. Table 1 shows a summary of the percent error for each quantity as compared to the experiment. The largest deviation from experimental results is the over-prediction of hydraulic efficiency for all three operating conditions. This is largely due to the exclusion of all secondary flow passages from the simulation. In the physical test, secondary flow passages such as the labyrinth seal introduce losses into the system. Omitting these passages from the simulation is a primary cause for the over-prediction of efficiency. It is important to note that the inclusion of these passages would further reduce the torque and discharge predictions.

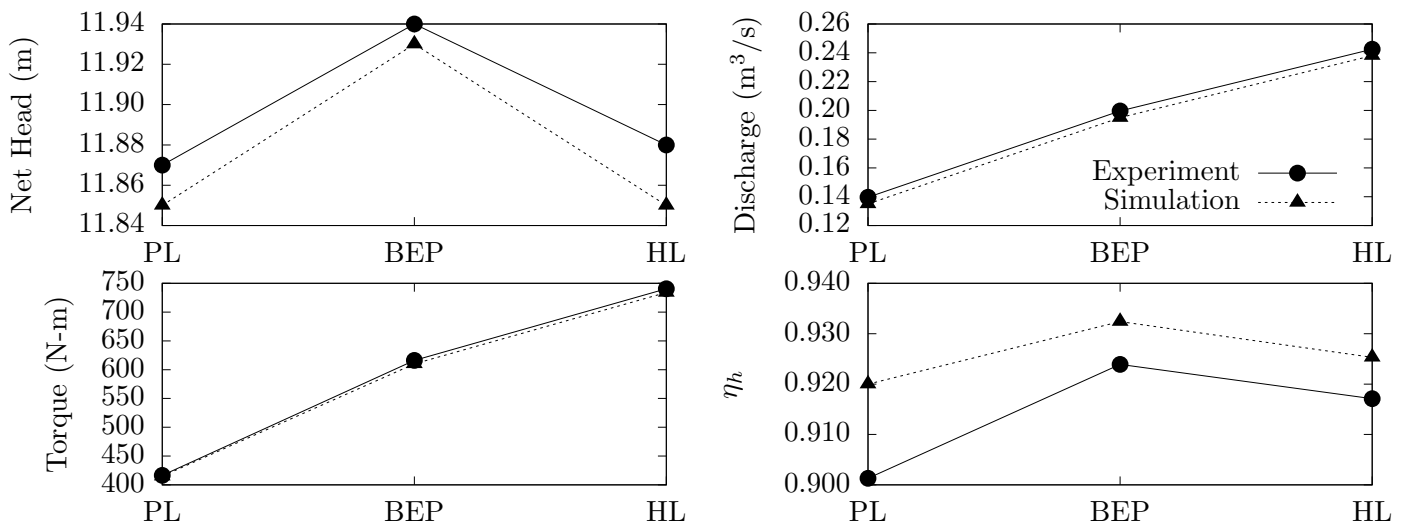


Figure 6: Predictions of quantities of interest for steady state operation

Table 1: Percent error of predicted integral quantities against reference experiment

Condition	Net Head	Discharge	Torque	Hydraulic Efficiency
PL	-0.17%	-3.31%	-0.33%	2.07%
BEP	-0.08%	-2.30%	-0.99%	0.92%
HL	-0.25%	-1.84%	-0.88%	0.89%

The reference experiment also provides velocity data along three lines in the draft tube. The locations of these sample lines are shown in Figure 3b. Velocity is measured in a coordinate

system that is centered with the runner axis and oriented as shown in the same figure. The probes are oriented in two different directions to provide two distinct pieces of information. As shown in Figure 3b, measurement lines L1 and L2 are oriented transverse to the draft tube, while L3 is aligned with the runner axis. The velocity profiles along L1 and L2 provide information on the size and strength of the vortex rope. Probe L3 characterizes how the strength of the vortex rope changes moving downstream from the runner. For the remainder of the results, the probe locations will be presented as a function of normalized position between 0 and 1. A normalized location of 0 is shown as a black square and a normalized location of 1 is shown as a white diamond in Figure 3b.

An investigation of the experimentally measured data is important to understand the length of the sample required for obtaining a mean flow-field. The measurements of velocity in the draft tube in the reference experiment show that there is a significant difference in frequency of oscillations for each condition. For averaging the simulation, we must at least run for a time equal to the period of the largest wavelength of oscillation from the experiment. This will ensure that flow features across all the relevant time-scales have been captured. The data shows that the lowest frequency of velocity measurement is shown in the PL case. This low frequency structure has a time-period of three runner revolutions so all velocity probe data is averaged over this period after reaching cycle steady convergence.

Comparing simulation data to the measured average velocities provides an indication of how well the flow features are predicted within the draft tube. The averaged velocity measurements from the experiment and simulation for the PL steady operating condition are shown in Figure 7. The predicted U velocity component is quite close to zero for all three measurement lines, which means that the flow is not strongly biased towards this Cartesian direction. The V velocity component provides some information about the shape of the vortex rope structure. The V velocity component trends show a large area of low velocity towards the center of the draft tube. This suggests a the presence of a large, unsteady vortex rope. Figure 10a illustrates the large size of the vortex core. Figure 12a also shows the existence of a large and unstructured vortex rope by presenting the time-averaged streamlines of the vortex rope. Predictions along L3 for V also highlight the quick reduction in the intensity of this vortex rope. Data for both velocity components correlates well with experimental measurements.

The averaged velocity probe measurements from the experiment and simulation for the BEP steady operating condition are shown in Figure 8. As was the case with the PL operating condition, the U velocity components for this case are close to zero for all three lines. Studying the V velocity trends shows a very narrow region of relatively low velocities near the center of the draft tube. This in turn suggests the existence of a narrow or 'tight' vortex rope. This is confirmed by the time averaged V velocity component contours shown in Figure 11b and the time-averaged streamlines of the vortex rope shown in Figure 12b. Probe L3 predictions for V show a weakening of this vortex as one moves downstream in the draft tube. In general, the CFD predictions correlate well with experiment, with the largest deviation being the under-prediction of the velocity magnitude in the axial direction.

The averaged velocity probe measurements from the experiment and simulation for the HL steady operating condition are shown in Figure 9. The simulation predicts a close to zero U velocity for all lines again, but the experiment suggests that there is some directionality for U for this operating condition. The experimental measurements show that the U velocity is slightly negative for each of the probes. The V velocity component predictions show the existence of a very strong vortex rope for this case. With both L1 and L2 probes, V almost reaches complete stagnation at the center of the draft tube. Compared to the BEP case, the vortex rope also appears to be slightly wider. This is clearly evidenced by the time averaged V velocity contours shown in Figure 11c and the time-averaged vortex rope streamlines shown in Figure 12c. The simulation predictions for the V velocity component match the experimental measurements quite

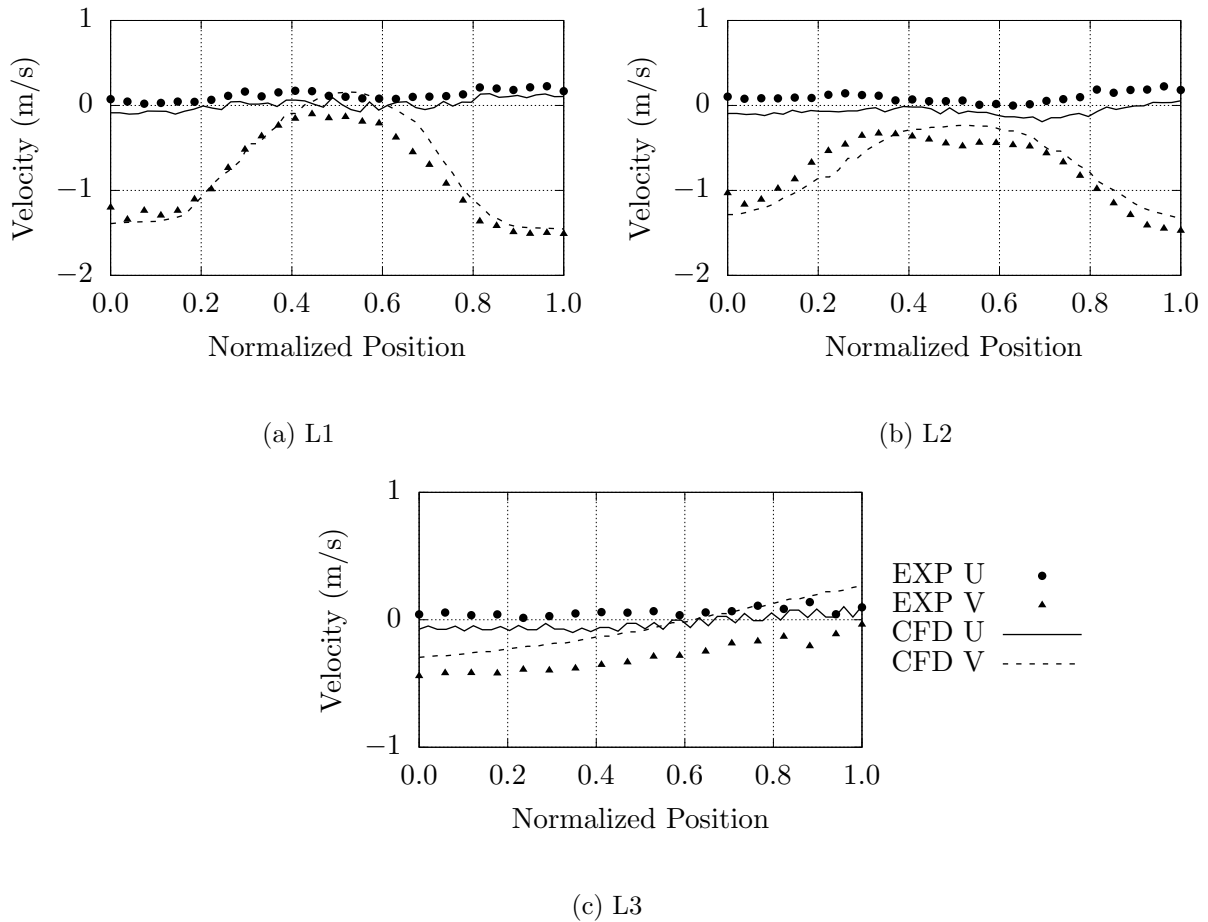


Figure 7: Simulation predictions and experimental results for averaged velocities in the draft tube for the PL operating condition

well.

4.2. Unsteady Operation

The unsteady operation of the turbine is the transient phenomenon in which the turbine changes between steady points of operation. The transient conditions studied in this study are: 1. Load acceptance (BEP to HL), and 2. Load reduction (BEP to PL). As mentioned in section 3.3, the inlet and outlet pressures are calculated as a temporal profile from the experimental data. The extracted quantities of interest are net head and discharge. The discharge measured in the experiment for both of these operating conditions is not accurate [12]. The experimentalists recommend to use a linear profile between the measurements for the two steady operating conditions. It is also important to note that the experimental reference suggests that the measurements of the key quantities may not be synced temporally with the guide vane rotation, so some artificial lead or lag is expected in the response.

Comparisons of the experimental and simulation measurements are shown in Figures 13 and 14 respectively. The simulation net head results follow the experimental measurements quite closely. The simulation prediction shows an abrupt change at the exact time when the guide vanes start their rotation (time = 1 sec). This abrupt change is not found in the experiment. This can be explained by the fact that the simulation is run with a constant density approach,

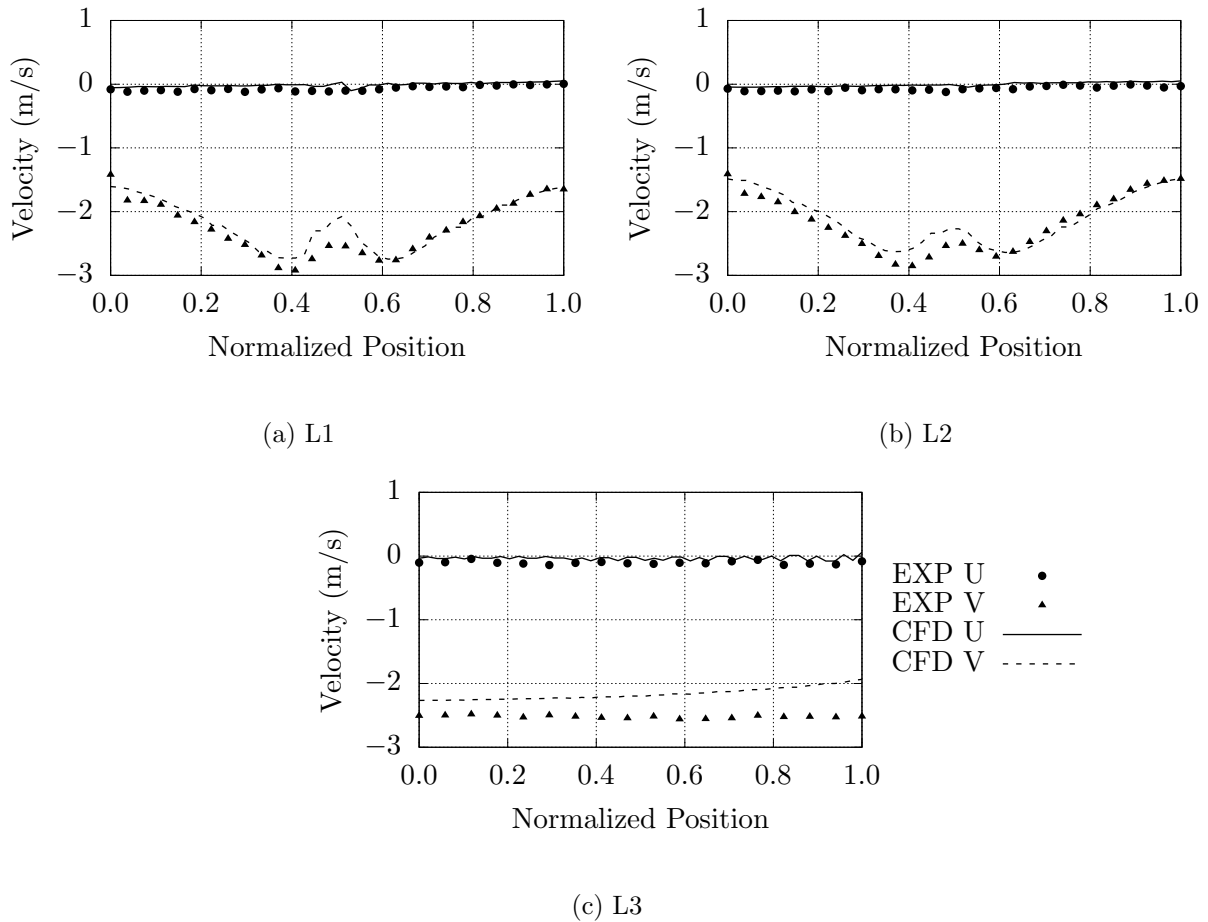


Figure 8: Simulation predictions and experimental results for averaged velocities in the draft tube for the BEP operating condition

therefore any discontinuity in simulation conditions causes an abrupt change everywhere in the domain. Adding compressibility to the modeling approach would help to absorb some of these effects (similar to actual operation). The amplitude of oscillations of net head is also under-predicted, but this is to be expected as explained in section 3.3. The discharge values show a linear profile during guide vane rotation. This follows the expected trend exactly as given by the experimentalists. The quantitative simulation measurements also track the experiment well. The slope of the linear profile is completely dependent on the start and final predictions of the simulation, i.e. a different slope is indicative of the steady operating conditions at the start and end of transient operation not being captured exactly. An estimate of discharge prediction error for steady operating conditions can be found in section 4.1.

5. Conclusions

Numerical predictions of the Francis-99 hydroturbine using the commercial CFD code STAR-CCM+ correlate well with experiment. All simulations use implicit unsteady time integration with rigid body motion to model runner rotation. An unstructured polyhedral mesh is able to accurately capture all geometric features and is well suited to modeling complex flow structures such as the vortex rope. Prism layer cells are used to resolve wall gradients, which is important to accurately predicting runner torque and, therefore, efficiency.

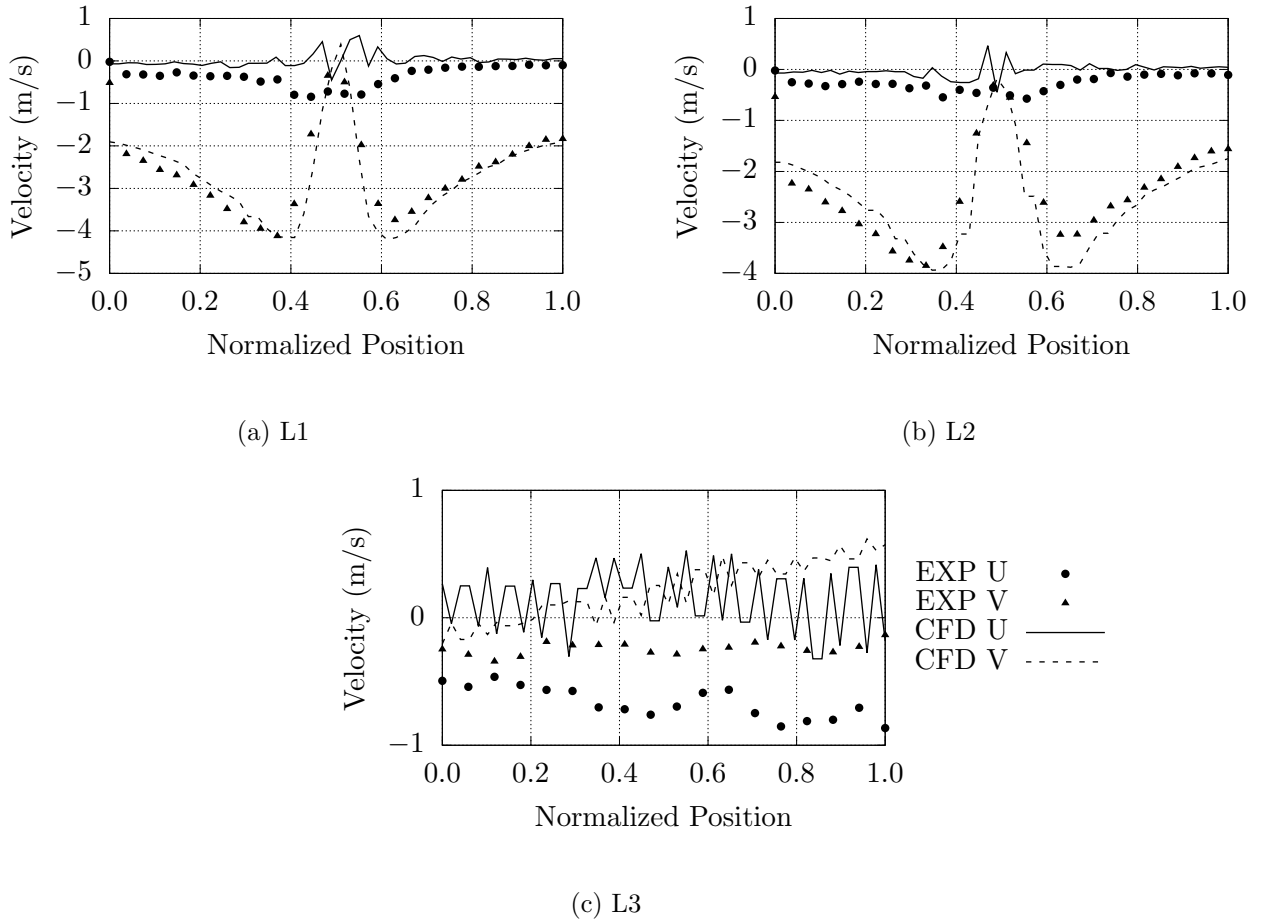


Figure 9: Simulation predictions and experimental results for averaged velocities in the draft tube for the HL operating condition

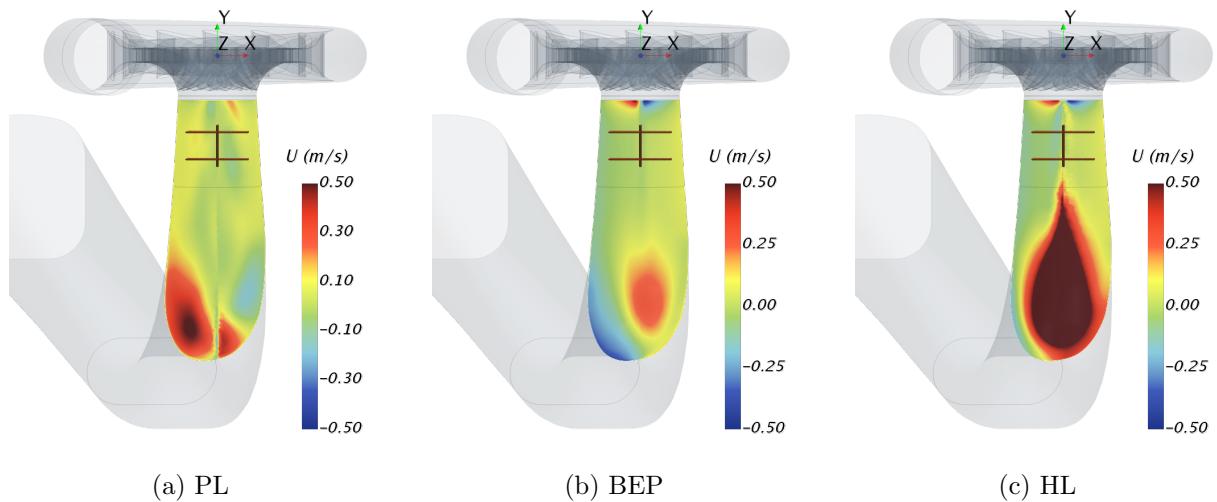


Figure 10: Time averaged U velocity contours for the steady operating conditions. The coordinate system shown is used for the velocity measurements.

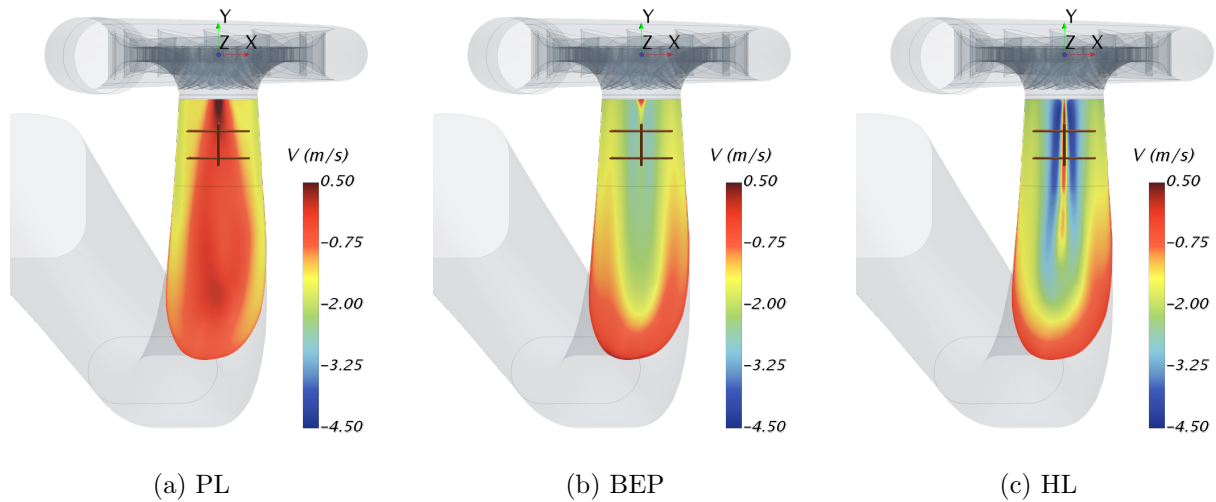


Figure 11: Time averaged V velocity contours for the steady operating conditions. The coordinate system shown is used for the velocity measurements.

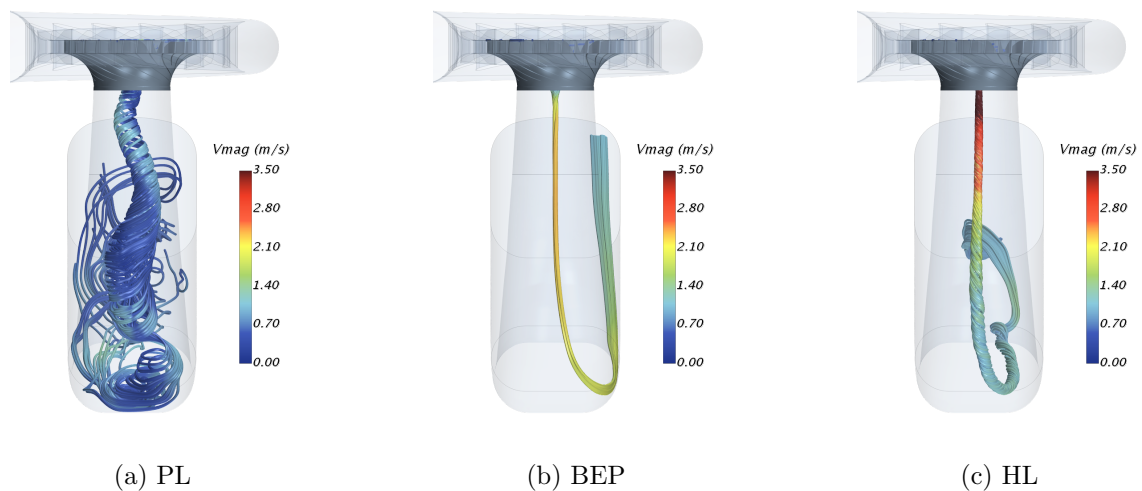


Figure 12: Time averaged streamlines of the vortex rope for the steady operating conditions

Steady operation was analyzed at BEP, PL and HL conditions. Net head, discharge, runner torque and hydraulic efficiency all correlate closely with experimentally observed values. Nearly all quantities are predicted within 3.5% of the experimental observation. Part load operation shows the greatest discrepancy. This operation condition contains the most complex flow features with many unsteady time-scales present.

Local velocity features of the flow-field are characterized downstream of the runner. The V velocity measured on lines transverse to the draft tube (L1 and L2) display the axial velocity defect due to the vortex structure. Both simulation and experiment show that this velocity defect is most pronounced for the HL case. The velocity defect observed for the BEP case is still present at the center of the passage, but does not show the same strength. The time-averaged V velocity observed for the part load case shows a much broader distribution of due to the large and unsteady nature of the vortex rope. U velocity profiles are much lower in magnitude and show minor levels of discrepancy for the off-design conditions.

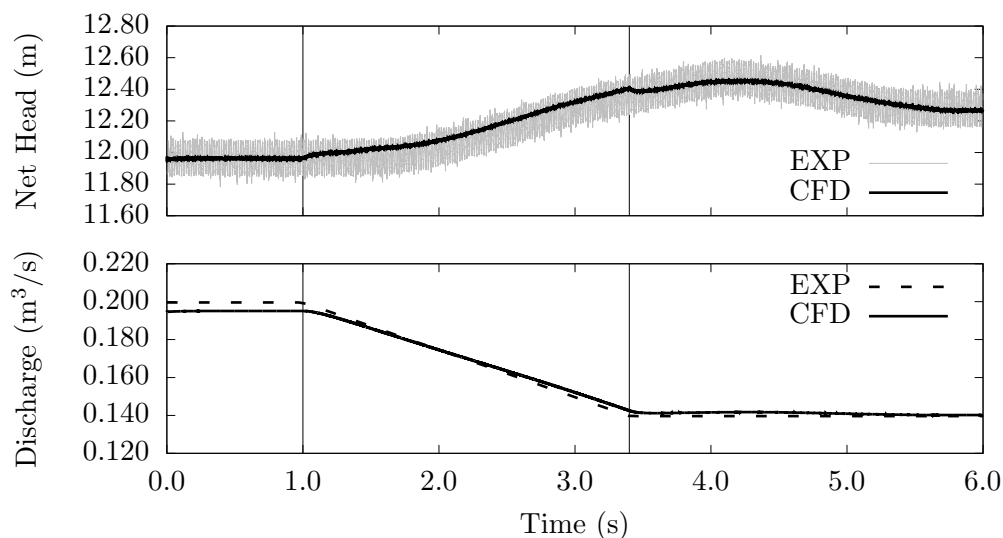


Figure 13: Net head and discharge results of the load reduction operating condition for the experiment and simulation. Vertical lines denote start and end of guide vane rotation.

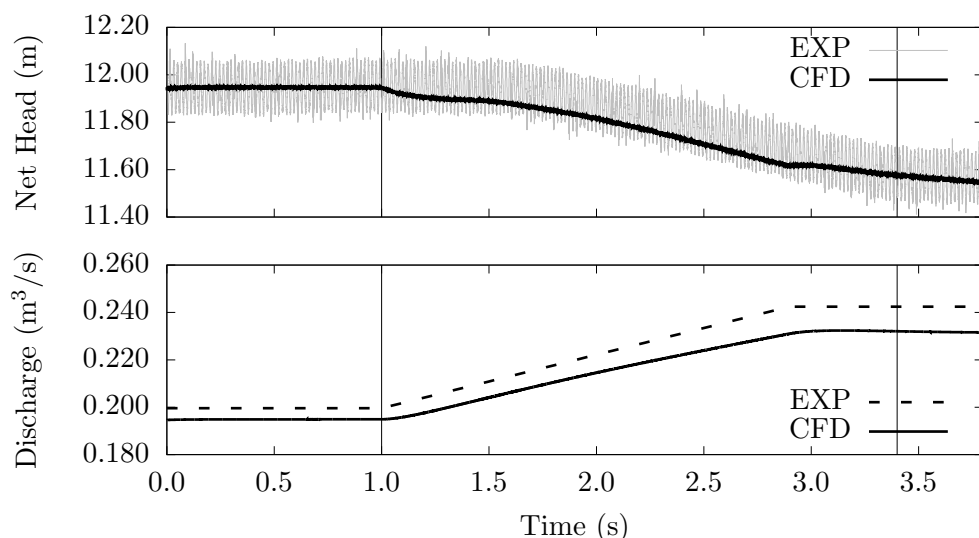


Figure 14: Net head and discharge results of the load acceptance operating condition for the experiment and simulation. Vertical lines denote start and end of guide vane rotation.

Velocity predictions aligned with the runner axis (L3) agree well with experiment for the BEP case. Velocities on L3 show higher levels of discrepancy for the PL and HL cases. A small vortex core is observed for the HL case. Conversely, the vortex structure associated with the PL condition is large, unsteady, and interacts strongly with the draft tube. This complex interaction impacts the relative agreement between simulation and experiment. Streamlines showing velocity magnitude are used to show the relative strength of the vortex rope and its interaction with the draft tube.

Unsteady simulation from BEP to HL and from BEP to PL was achieved using grid morphing to physically move the guide vanes as a function of time. Both the overall predicted values and unsteady trends agree with experiment. Notably, simulation predicts a sharp change in predicted values at the start and end of guide vane rotation. This is likely due to three factors. First, the fluid was modeled as strictly incompressible, where the physical system will include a small

level of compressibility. Second, the simulation domain does not encompass the entire test loop and constant-value boundary conditions are applied. Finally, the function used to specify the vane rotation is non-differentiable, whereas it is likely that the rotation profile imposed in the experiment was smooth.

Once properly validated, simulation is able to accurately predict overall machine performance for both steady and unsteady operation. Additionally, detailed insight into flow-field characteristics offer insight on how turbines may be better designed and where experimental measurements may be taken to be of highest value. Simulation provides an accessible platform for repeatable analysis of machines and can enable design-space exploration, sensitivity analysis, and detailed understanding of in situ operation.

Turbulence models better able to model anisotropic flows such as the vortex rope often outperform more computationally efficient models such as the $k-\omega$ SST model used in this study. A sensitivity to turbulence model with a baseline Large Eddy Simulation (LES) will be performed.

With a turbulence model that is better able to model the complex flow structures of the vortex rope, the long time-scale flow features of the draft tube will be more fully characterized to understand driving factors and how these features impact performance. In support of this effort, it will likely be necessary to extend the computational domain to remove constraints from the system.

References

- [1] Renewables 2016 global status report.
- [2] Jacek Swiderski, Joseph N Martin, and Richard Norrena. Automated runner blade design optimization process based on cfd verification. *parameters*, 11:n11, 2001.
- [3] Jingchun Wu, Katsumasa Shimmei, Kiyohito Tani, Kazuo Niikura, and Joushirou Sato. Cfd-based design optimization for hydro turbines. *Journal of Fluids Engineering*, 129(2):159–168, 2007.
- [4] P Drtina and M Sallaberger. Hydraulic turbines basic principles and state-of-the-art computational fluid dynamics applications. *Proceedings of the Institution of Mechanical Engineers, Part C: Journal of Mechanical Engineering Science*, 213(1):85–102, 1999.
- [5] Sanjay Jain, RP Saini, and Arun Kumar. Cfd approach for prediction of efficiency of francis turbine. In *The 8th International Conference on Hydraulic Efficiency Measurement*, 2010.
- [6] Santiago La´n Beatove, Manuel J Garc´a Ruiz, Brian Quintero Arboleda, and Santiago Orrego Bustamante. Cfd numerical simulations of francis turbines. *Revista Facultad de Ingenier´a*, (51):31–40, 2013.
- [7] Manoj Kumar Shukla, Rajeev Jain, Vishnu Prasad, and S Shukla. Cfd analysis of 3-d flow for francis turbine. *Int. J. Mech. Eng*, 2:93–100, 2011.
- [8] MV Magnoli. Numerical simulation of pressure oscillations in francis turbine runners. *JASS Numerical Simulation of Turbomachinery*, pages 32–50, 2009.
- [9] Chirag Trivedi, Michel J Cervantes, BK Gandhi, and Ole G Dahlhaug. Experimental and numerical studies for a high head francis turbine at several operating points. *Journal of Fluids Engineering*, 135(11):111102, 2013.
- [10] Kenji Shingai, Nobuaki Okamoto, Yuta Tamura, and Kiyohito Tani. Long-period pressure pulsation estimated in numerical simulations for excessive flow rate condition of francis turbine. *Journal of Fluids Engineering*, 136(7):071105, 2014.
- [11] Starccm+® — cfd simulation software. <http://www.cd-adapco.com/products/star-ccm%C2%AE>. Accessed: 2016-09-13.
- [12] Norwegian Hydropower Center. Francis-99. <https://www.ntnu.edu/nvks/francis-99>. Accessed: 2016-09-15.
- [13] Milovan Peric. Flow simulation using control volumes of arbitrary polyhedral shape. *ERC OFTAC Bulletin*, 62, September 2004.
- [14] International Electrotechnical Commission. Hydraulic turbines, storage pumps and pump-turbines: Model acceptance tests. Technical Report IEC 60193, 3, rue de Varemb, PO Box 131, CH-1211 Geneva 20, Switzerland, 1999. Second Edition.
- [15] Sir Maurice Kendall, Alan Stuart, and J. Keith. Ord. *The advanced theory of statistics*. Oxford University Press, 1983.
- [16] Colin Heye. Introduction to overset mesh with star-ccm+. In *13th Symposium on Overset Composite Grids and Solution Technology*, October 2016.